

Time-dependent numerical methods for the quantum hydrodynamic model for semiconductor devices

Carl L. Gardner (✉ Carl.Gardner@asu.edu)

Arizona State University

Research Article

Keywords: resonant tunneling diode, quantum hydrodynamics, time-dependent methods

Posted Date: May 27th, 2022

DOI: <https://doi.org/10.21203/rs.3.rs-1670643/v1>

License:  This work is licensed under a Creative Commons Attribution 4.0 International License.

[Read Full License](#)

Time-dependent numerical methods for the quantum hydrodynamic model for semiconductor devices

Carl L. Gardner

Received: date / Accepted: date

Abstract Numerical methods are developed for the time-dependent smooth quantum hydrodynamic (QHD) model for semiconductor devices by solving the underlying hyperbolic gas dynamical part of the transport equations with a third-order WENO method, treating the quantum mechanical terms as source terms; the parabolic heat conduction term using the TRBDF2 method; and the elliptic Poisson equation using PCG. These are the first time-dependent simulations of the smooth QHD model, and the first time-dependent simulations of any QHD model at 300 K. Time-dependent simulations of the resonant tunneling diode to steady state are presented, which show realistic negative differential resistance (the experimental signal of quantum resonance) in the current-voltage curve.

Keywords resonant tunneling diode · quantum hydrodynamics · time-dependent methods

1 Introduction

Quantum semiconductor devices including resonant tunneling diodes [8], quantum field effect transistors [14, 18], high electron mobility transistors [15], and super-lattice devices, etc., with applications to multiple-state logic and memory devices and high frequency oscillators and sensors, can be efficiently simulated by incorporating quantum terms into a hydrodynamical description [17, 1] of charge propagation.

In this investigation, we apply the time-dependent *smooth* quantum hydrodynamic (QHD) model [9] to simulating neg-

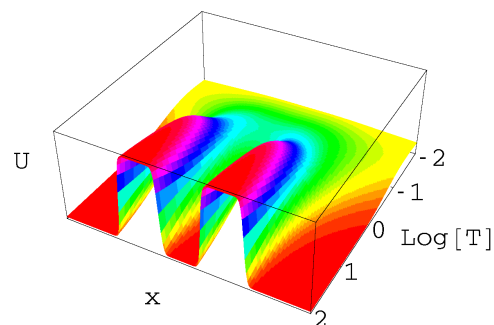


Fig. 1 Smooth barrier potential U_B for electrons in GaAs for unit double barriers vs. $\log_{10}(T/(300 \text{ K}))$ and x . The barriers are 5 nm wide and the quantum well between the barriers is also 5 nm wide.

ative differential resistance¹ (NDR)—the experimental signal of quantum resonance—for the resonant tunneling diode.

The smooth QHD model invokes a smoothing of the classical potential energy over both space and inverse temperature $\beta = 1/T$, creating a residual smooth potential with a lower potential height in the barrier regions (see Fig. 1). Note that the effective barrier height $\rightarrow 0$ as the ambient temperature $T \rightarrow 0$, and the effective range of the barriers $\rightarrow \infty$. These effects explain why particle tunneling is enhanced at low temperatures. As $T \rightarrow \infty$, the smooth potential approaches the localized classical double barrier potential and quantum effects are suppressed.

We present here the first time-dependent smooth QHD simulation results in the literature, and the first time-dependent simulations of any QHD model at 300 K. The splitting method employed in [5] for time-dependent simulations of the origi-

C. L. Gardner
School of Mathematical & Statistical Sciences
Arizona State University, Tempe, AZ, USA
email: Carl.Gardner@asu.edu

¹ A region in the current-voltage curve where the current *decreases* as the voltage *increases*.

nal QHD model will be modified and extended to the smooth QHD model, using the third-order WENO method for the gas dynamical propagation and the implicit TRBDF2 method (rather than an explicit method, allowing for larger timesteps) for heat conduction.

2 Smooth QHD model equations

The smooth QHD equations take the same form as the classical hydrodynamic equations for conservation of mass (particle number), momentum, and energy, respectively (for simplicity we just treat electrons here):

$$\frac{\partial}{\partial t}(mn) + \frac{\partial}{\partial x_i}(mnu_i) = 0 \quad (1)$$

$$\frac{\partial}{\partial t}(mnu_j) + \frac{\partial}{\partial x_i}(mnu_i u_j - P_{ij}) = -n \frac{\partial V}{\partial x_j} - \frac{mnu_j}{\tau_p} \quad (2)$$

$$\frac{\partial W}{\partial t} + \frac{\partial}{\partial x_i}(u_i W - u_j P_{ij} + q_i) = -nu_i \frac{\partial V}{\partial x_i} - \frac{(W_{cl} - \frac{3}{2}nT_0)}{\tau_w} \quad (3)$$

where m is the effective electron mass, n is the electron density, mn is the electron mass density, u_i is the velocity, mnu_i is the momentum density, P_{ij} is the stress tensor, V is the classical potential energy, W is the total (classical plus quantum) energy density, $W_{cl} = \frac{3}{2}nT + \frac{1}{2}mnu^2$ is the classical energy density, T is the temperature of the electron gas, and q_i is the generalized heat flux. Boltzmann's constant k_B has been set to 1. Indices i, j equal 1, 2, 3, and repeated indices are summed over. Electron scattering is modeled by the standard relaxation time approximation, with momentum and energy relaxation times τ_p and τ_w .

The conserved variables (which are used in the numerical code described below) for gas dynamics are mass density $\rho = mn$, momentum density $p_i = mnu_i$, and total (classical plus quantum) energy density W . It is also possible to formulate the equations with conserved variables mass density, momentum density, and classical energy density W_{cl} , where the energy conservation equation (3) has an additional source term, but the computational results are more robust using the total energy density W as the conserved variable.

The transport equations (1)–(3) are coupled to Poisson's equation for the electrostatic potential energy V_P :

$$\nabla \cdot (\epsilon \nabla V_P) = e^2 (N_D - N_A - n), \quad V_P = -e\phi \quad (4)$$

where ϕ is the electrostatic potential, $e > 0$ is the electronic charge, ϵ is the dielectric constant, N_D is the density of donors, and N_A is the density of acceptors ($N_A = 0$ for the device simulated here). The total potential energy V consists of two parts, one from Poisson's equation V_P and the other from the potential barriers V_B :

$$V = V_B + V_P. \quad (5)$$

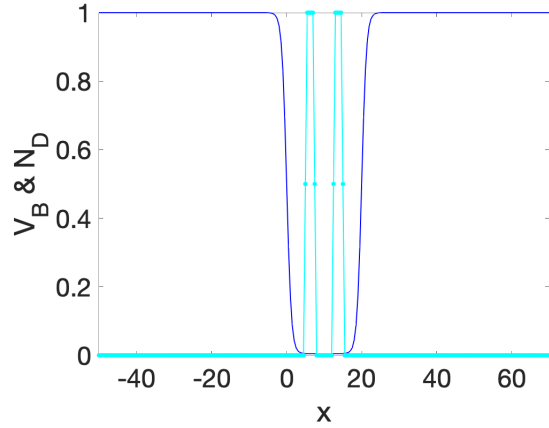


Fig. 2 Doping density N_D (blue) in 10^{18} cm^{-3} and double barriers V_B/B (cyan), where B is the barrier height, for the resonant tunneling diode vs. x in nm. The channel is 20 nm long, the barriers are 2.5 nm wide, and the quantum well between the barriers is 5 nm wide. There are 5 nm spacers between the barriers and the contacts. In Figs. 2 and 3, dots indicate grid point values for 240 Δx .

V_B has a step function discontinuity at potential barriers (see Fig. 2).

Quantum effects enter into the expressions for the stress tensor P_{ij} , energy density W , and generalized heat flux q_i . The quantum contributions to the stress tensor and energy density are proportional to the square of the *thermal Planck constant* \hbar_β , with

$$\hbar_\beta^2 \equiv \frac{\hbar^2 \beta}{4m} = \frac{\hbar^2}{4mT_0} \approx \begin{cases} (3.42 \text{ nm})^2 & 300 \text{ K} \\ (6.75 \text{ nm})^2 & 77 \text{ K} \end{cases} \quad (6)$$

where $\beta \equiv 1/T_0$ and the numerical values are for GaAs. The quantum contribution to q_i is independent of temperature and is proportional to \hbar^2 .

The stress tensor and energy density are

$$P_{ij} = -nT \delta_{ij} - \hbar_\beta^2 n \frac{\partial^2 \bar{V}}{\partial x_i \partial x_j} \quad (7)$$

$$W = \frac{3}{2}nT + \frac{1}{2}mnu^2 + \frac{1}{2}\hbar_\beta^2 n \nabla^2 \bar{V} \quad (8)$$

where nT is the pressure P and \bar{V} is the *quantum potential*, given by

$$\bar{V}(\beta, \mathbf{x}) = \int_0^\beta \frac{d\beta'}{\beta} \left(\frac{\beta'}{\beta} \right)^2 \times \int d^3 x' \left(\frac{2m\beta}{\pi(\beta - \beta')(\beta + \beta')\hbar^2} \right)^{3/2} \times \exp \left\{ -\frac{2m\beta}{(\beta - \beta')(\beta + \beta')\hbar^2} (\mathbf{x}' - \mathbf{x})^2 \right\} V(\mathbf{x}'). \quad (9)$$

Note the double smoothing over both space and (inverse) temperature.

We have found that a *computational viscosity* term is needed on the right-hand side of the conservation of momentum equation (2) for the resonant tunneling diode simulations in Section 4 to converge to steady state:

$$\begin{aligned} \frac{\partial}{\partial t}(mnu_j) + \frac{\partial}{\partial x_i}(mnu_i u_j - P_{ij}) = \\ -n \frac{\partial V}{\partial x_j} - \frac{mnu_j}{\tau_p} + \nu \frac{\partial^2}{\partial x_j \partial x_i}(mnu_i) \end{aligned} \quad (10)$$

where ν is the computational viscosity coefficient. Without the viscosity term, sound waves bounce around in the double-barrier channel essentially “forever” and prevent convergence to steady state for barrier heights $B > 0.05$ eV. Various attempts at smoothing or filtering the computed solutions or derivatives to damp out the sound waves eliminated any NDR. The sound waves are largely confined to the channel quantum structures, so absorbing boundary conditions at the left source boundary and/or at the right drain boundary do not help in this context. In steady state, the computational viscosity term goes to zero by virtue of the mass conservation equation (1). Physical viscosity (unlike heat conduction) in an electron gas in a semiconductor is negligibly small—physical viscosity terms in the stress tensor P_{ij} give unphysical results. A *numerical* viscosity term in the momentum conservation equation (2) (in which $\nu \rightarrow 0$ as Δt and $\Delta x \rightarrow 0$) is too small to eliminate the transient sound waves. The computational viscosity mechanism rapidly achieves steady state by damping out the transient sound waves in the channel, and vanishes as steady state is attained.

2.1 Quantum and smooth potentials

In general, the quantum potential involves a smoothing of $V_B + V_P$, but since V_P is already smooth for the resonant tunneling diode simulations presented below, and since in addition the contribution of V_P to the quantum potential is much smaller in magnitude than the contribution of V_B , we consider just the smoothing of V_B . The contribution of V_P to the quantum potential does not affect the current-voltage curve to more than a line width for the resonant tunneling diode considered here.

Only second spatial derivatives of \bar{V}_B appear in P_{ij} and W . For the 1D resonant tunneling diode,

$$V_B = B(\theta(x - x_1) - \theta(x - x_2) + \theta(x - x_3) - \theta(x - x_4)) \quad (11)$$

where B is the barrier height, θ is the unit step function from 0 to 1, and x_1 (x_3) and x_2 (x_4) label the left and right barrier edges of the first (second) barrier, respectively. The x' integration for $d^2\bar{V}_B/dx^2$ can be performed, yielding

$$\frac{d^2\bar{V}_B}{dx^2} = -\frac{B}{\sqrt{2\pi}\hbar^3} \int_0^b \frac{db b^2}{(1-b^2)^{3/2}} \times$$

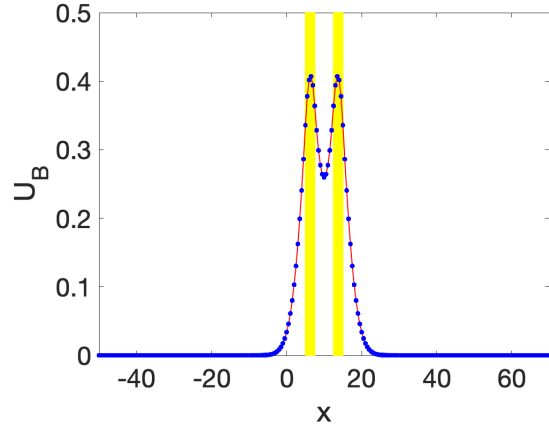


Fig. 3 Smooth barrier potential U_B/B for the resonant tunneling diode at 300 K vs. x in nm. In this and subsequent figures, the vertical yellow bands indicate the locations of the double barriers.

$$\begin{aligned} & \left((x - x_1) \exp \left\{ -\frac{(x - x_1)^2}{2\hbar_\beta^2(1 - b^2)} \right\} - \right. \\ & (x - x_2) \exp \left\{ -\frac{(x - x_2)^2}{2\hbar_\beta^2(1 - b^2)} \right\} + \\ & (x - x_3) \exp \left\{ -\frac{(x - x_3)^2}{2\hbar_\beta^2(1 - b^2)} \right\} - \\ & \left. (x - x_4) \exp \left\{ -\frac{(x - x_4)^2}{2\hbar_\beta^2(1 - b^2)} \right\} \right). \end{aligned} \quad (12)$$

Then the b integration is calculated at each x just once at $t = 0$ at the beginning of the simulation.

The *smooth* combination for the double barriers that appears in the momentum (2) and energy (3) conservation equations

$$U_B = V_B + \hbar_\beta^2 \frac{d^2\bar{V}_B}{dx^2} \quad (13)$$

is presented in Fig. 3 for the double barriers at 300 K analyzed in this investigation. Note that V_B , \bar{V}_B , and U_B are linear in the barrier height B . U_B is two degrees smoother [10] than the barrier potential V_B ; i.e., if V_B has a step function discontinuity, U_B is once differentiable. The effective barrier height in the smooth barrier potential U_B is only 40% of the barrier height, enhancing electron transmission through the barrier.

2.2 Models and parameters

The generalized heat flux (derived through the Chapman-Enskog expansion for the moments of the Wigner-Boltzmann equation in [10])

$$\mathbf{q} = -\kappa \nabla T - \frac{\hbar^2 n}{8m} \nabla^2 \mathbf{u} \quad (14)$$

includes both a classical and a quantum term, and incorporates important effects of the higher moments of the Wigner-Boltzmann equation that are omitted in the fluid dynamical approximation. The dispersive quantum term $\frac{\hbar^2}{8m} \nabla \cdot (n \nabla^2 \mathbf{u})$ in $-\nabla \cdot \mathbf{q}$ may be included or not, depending on modeling issues. For the resonant tunneling diode simulated here, more NDR is produced *without* the quantum heat conduction term.

We model the relaxation times τ_p and τ_w by modified Baccarani-Wordeman [2] models

$$\tau_p = m\mu_{n0} \frac{T_0}{T} \equiv \tau_{p0} \frac{T_0}{T}, \quad \tau_w = \frac{\tau_p}{2} \left(1 + \frac{\frac{3}{2}T}{\frac{1}{2}mv_s^2} \right) \quad (15)$$

and the coefficient κ by

$$\kappa = \kappa_0 \mu_{n0} n T_0 \equiv \bar{\kappa} n \quad (16)$$

where μ_{n0} is the low-field electron mobility, v_s is the electron saturation velocity, and $\kappa_0 > 0$ is a dimensionless phenomenological constant.

3 Time-dependent numerical methods

The main prediction needed by semiconductor device modelers is the steady-state current-voltage curve of a particular device (classical or quantum diode or transistor). A steady-state solution and output current are computed for each (constant) voltage configuration.

The smooth QHD equations (1)–(4) can be solved in steady-state by using either a steady-state Newton solver [6] or by simulating the time-dependent equations to steady state (see [5] for the original QHD model). In 1D, directly solving the steady-state equations with a damped Newton method is efficient and robust, but in 2D and 3D the cost of the linear solves within the Newton method becomes prohibitive. The most efficient technique then in 2D and 3D is to solve the time-dependent equations to steady state. Time-dependent problems are also of intrinsic interest: e.g., a time-varying voltage bias $V_{bias}(t)$ may be applied across a device, yielding time-varying solutions.

We solve the underlying hyperbolic gas dynamical part of the time-dependent smooth QHD equations using the third-order WENO method [16], treating the quantum mechanical, electric field, and relaxation time terms as source terms; the parabolic heat conduction and computational viscous terms using the TRBDF2 [3] method; and the elliptic Poisson equation using PCG.

This type of technique was successfully applied to the original QHD model in [5] to simulate the 1D resonant tunneling diode at 77 K, using a Runge-Kutta/discontinuous Galerkin method for the hyperbolic solver and a mixed finite element method for the source terms and Poisson's equation. As yet, there have been no 2D or 3D QHD simulations, and

there are no time-dependent smooth QHD simulation results in the literature—there are only 2D or 3D simulations of much simpler models like the density-gradient model [18] or the quantum drift-diffusion model (see for example [4, 12–15]), which omit the energy conservation equation (3) by assuming devices are at a constant (ambient) temperature. The current-voltage curves for modern submicron devices for these models have little resemblance to actual experimentally measured current-voltage curves, because electrons and holes in submicron classical and quantum mechanical devices have wide temperature variations (see Fig. 7 for the resonant tunneling diode).

In addition, classical and quantum hydrodynamic simulations of submicron devices involve supersonic flow, where hyperbolic methods are crucial. Classical and quantum drift-diffusion models are parabolic, and omit these important physical effects.

Reference [5] used an explicit solver for the parabolic heat conduction term, which severely limited the timestep size. The implicit TRBDF2 method is A-stable and L-stable, so timesteps are only restricted by desired accuracy, and relatively large timesteps can be taken for the heat conduction and computational viscous terms based on the CFL timestep constraint for the gas dynamical solver.

3.1 WENO

ENO (essentially non-oscillatory) and WENO (weighted essentially non-oscillatory) [16] are high-order upwind methods designed for nonlinear hyperbolic conservation laws with piecewise smooth solutions containing sharp discontinuities like shock waves and contacts. Here we use a third-order finite difference version of WENO with Lax–Friedrichs flux splitting (WENO3-LF). In 1D, we choose locally smooth stencils which avoid crossing discontinuities whenever possible. WENO uses a convex combination of all candidate stencils, rather than just one as in the original ENO method.

To describe the third-order WENO scheme in more detail, we begin with a 1D scalar equation

$$w_t + f(w)_x = 0 \quad (17)$$

and assume $\partial f(w)/\partial w \geq 0$, i.e., that the “wind direction” is positive. The computational domain is discretized into $N + 1$ grid points $x_j = j\Delta x$, $j = 0, 1, 2, \dots, N$, where Δx is the grid spacing. A conservative numerical approximation $w_j(t)$ to the exact solution $w(x_j, t)$ of (17) takes the following form:

$$\frac{dw_j(t)}{dt} + \frac{1}{\Delta x} (F_{j+\frac{1}{2}} - F_{j-\frac{1}{2}}) = 0 \quad (18)$$

where $F_{j+\frac{1}{2}}$ is the *numerical flux*. For the third-order WENO scheme, the numerical flux is

$$F_{j+\frac{1}{2}} = \omega_1 F_{j+\frac{1}{2}}^{(1)} + \omega_2 F_{j+\frac{1}{2}}^{(2)} \quad (19)$$

where $F_{j+\frac{1}{2}}^{(m)}$, $m = 1, 2$, are the two second-order accurate fluxes on two different stencils given by

$$F_{j+\frac{1}{2}}^{(1)} = -\frac{1}{2}f_{j-1} + \frac{3}{2}f_j, \quad F_{j+\frac{1}{2}}^{(2)} = \frac{1}{2}f_j + \frac{1}{2}f_{j+1} \quad (20)$$

where f_j denotes $f(w_j(t))$. The nonlinear weights are

$$\omega_m = \frac{\tilde{\omega}_m}{\sum_{l=1}^2 \tilde{\omega}_l}, \quad \tilde{\omega}_l = \frac{\gamma_l}{(\delta + \beta_l)^2} \quad (21)$$

with the linear weights

$$\gamma_1 = \frac{1}{3}, \quad \gamma_2 = \frac{2}{3} \quad (22)$$

and the smoothness indicators

$$\beta_1 = (f_j - f_{j-1})^2, \quad \beta_2 = (f_{j+1} - f_j)^2. \quad (23)$$

The parameter δ ensures that the denominator in (21) never becomes 0, and is fixed at $\delta = 10^{-6}$ in the computations presented here. (Numerical errors can be much lower than δ , approaching machine zero.) Note that the stencil for the scheme is biased to the left due to the upwinding.

If the wind direction $\partial f(w)/\partial w \leq 0$, the method for computing the numerical flux $F_{j+\frac{1}{2}}$ is the exact mirror image with respect to the point $x_{j+\frac{1}{2}}$ of the description above. The stencil is then be biased to the right. If $\partial f(w)/\partial w$ changes sign, we use a smooth flux splitting

$$f(w) = f^+(w) + f^-(w) \quad (24)$$

where $\partial f^+(w)/\partial w \geq 0$ and $\partial f^-(w)/\partial w \leq 0$, and apply the WENO procedure separately on $f^+(w)$ and $f^-(w)$. We recommend the Lax-Friedrichs flux splitting

$$f^\pm(w) = \frac{1}{2}(f(w) \pm \alpha w) \quad (25)$$

with $\alpha = \max_w |\partial f(w)/\partial w|$.

For multiple spatial dimensions, the finite-difference versions of WENO simply apply the WENO procedure in each direction to obtain high-order approximations to the relevant spatial derivatives. Unlike dimensional splitting, such a dimension by dimension splitting obtains high-order accuracy without the computational cost of fully multidimensional reconstructions.

The time discretization is implemented via a third-order TVD Runge-Kutta method:

$$\begin{aligned} w^{(1)} &= w^n + \Delta t L(w^n, t^n) \\ w^{(2)} &= \frac{3}{4}w^n + \frac{1}{4}w^{(1)} + \frac{1}{4}\Delta t L(w^{(1)}, t^n + \Delta t) \\ w^{n+1} &= \frac{1}{3}w^n + \frac{2}{3}w^{(2)} + \frac{2}{3}\Delta t L(w^{(2)}, t^n + \Delta t/2) \end{aligned} \quad (26)$$

where $L = L(w, t)$ is the approximation of the spatial derivatives $-\partial f(w)/\partial x$ by the WENO procedure.

A CFL condition is necessary for stability:

$$\alpha \frac{\Delta t}{\Delta x} \leq CFL \leq 1 \quad (27)$$

where α is the largest eigenvalue in magnitude of the Jacobian $\partial f(w)/\partial w$.

3.2 TRBDF2

TRBDF2 (trapezoidal rule plus second-order backward difference formula) [3] is a composite one-step method which is second-order accurate and L-stable. In the overall splitting method, both the heat conduction and computational viscous terms involve linear parabolic PDE corrections to the conserved variables (updating T and thereby W for heat conduction, and mnu for the computational viscosity).

Discretize the heat conduction or computational viscous term contribution in space as $dw/dt = f(w)$, with w now the vector of grid point values w_j . To integrate $dw/dt = f(w)$ from t_n to $t_{n+1} = t_n + \Delta t$, we first apply the trapezoidal rule (TR) to advance the solution from t_n to $t_{n+\gamma} = t_n + \gamma\Delta t$:

$$w_{n+\gamma} - \gamma \frac{\Delta t}{2} f_{n+\gamma} = w_n + \gamma \frac{\Delta t}{2} f_n, \quad (28)$$

and then use the second-order backward differentiation formula (BDF2) to advance the solution to t_{n+1} :

$$w_{n+1} - \frac{1-\gamma}{2-\gamma} \Delta t f_{n+1} = \frac{1}{\gamma(2-\gamma)} w_{n+\gamma} - \frac{(1-\gamma)^2}{\gamma(2-\gamma)} w_n. \quad (29)$$

This composite one-step method is second-order accurate and L-stable. To minimize the norm of the local error, γ is set to $2 - \sqrt{2} \approx 0.59$.

3.3 PCG

Poisson's equation (4) is solved with the standard preconditioned conjugate gradient (PCG) method with incomplete Cholesky factorization preconditioner.

4 Simulations of the resonant tunneling diode

We will solve the 1D time-dependent smooth QHD equations for the resonant tunneling diode with the conserved variables mass density mn , momentum density mnu , and total energy density W :

$$V = V_B + V_P, \quad U = V + \hbar_\beta^2 \bar{V}_{xx}, \quad \bar{V}_{xx} \approx \bar{V}_{Bxx} \quad (30)$$

$$W = \frac{3}{2}nT + \frac{1}{2}mnu^2 + \frac{1}{2}\hbar_\beta^2 n \bar{V}_{xx}, \quad W_{cl} = \frac{3}{2}nT + \frac{1}{2}mnu^2 \quad (31)$$

$$(mn)_t + (mnu)_x = 0 \quad (32)$$

$$\begin{aligned} (mnu)_t + (mnu^2 + nT)_x = \\ -nU_x - \hbar_\beta^2 n_x \bar{V}_{xx} + v(mnu)_{xx} - \frac{mnu}{\tau_p} \end{aligned} \quad (33)$$

$$\begin{aligned} W_t + (u(W + nT))_x = \\ -nuU_x - \hbar_\beta^2 (nu)_x \bar{V}_{xx} + \bar{\kappa}(nT_x)_x - \frac{W_{cl} - \frac{3}{2}nT_0}{\tau_w} \end{aligned} \quad (34)$$

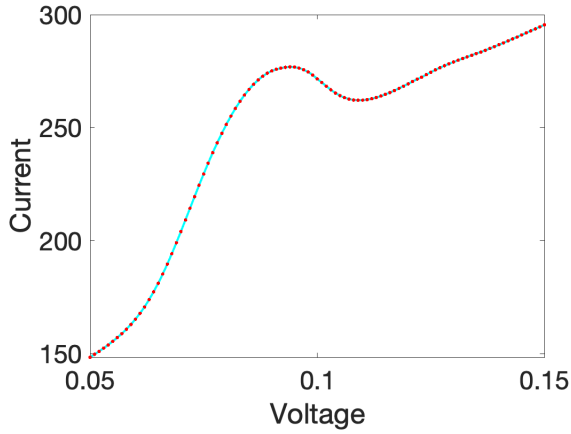


Fig. 4 Current in kA/cm^2 vs. applied voltage in volts for the resonant tunneling diode at 300 K with a 5 nm quantum well and 2.5 nm 280 meV quantum barriers.

$$V_{Pxx} = \frac{e^2}{\epsilon} (N_D - n). \quad (35)$$

For the current-voltage curve of the resonant tunneling diode, we simulate the time-dependent equations to steady state for each applied voltage V_{bias} across the device, using continuation in V_{bias} . Note that here we have set the dispersive quantum heat conduction term $\hbar^2 (nu_{xx})_x / (8m)$ to zero.

Equation (32) is hyperbolic with characteristic velocity u , equations (33) and (34) form a parabolic pair of equations due to the combination of heat conduction, quantum, and viscous terms (see [11]), and Poisson's equation (35) is elliptic, so seven boundary conditions are required, four at the left inflow boundary and three at the right outflow boundary. Seven physically relevant, well-posed boundary conditions are

$$\begin{aligned} n(x_L) &= N_D(x_L), & u_x(x_{L,R}) &= 0, & T_x(x_{L,R}) &= 0, \\ V_P(x_L) &= 0, & V_P(x_R) &= -eV_{bias} \end{aligned} \quad (36)$$

where x_L and x_R denote the left and right boundaries, respectively, of the resonant tunneling diode.

Smooth QHD simulations with $240 \Delta x$ of a GaAs resonant tunneling diode at 300 K with AlGaAs double barriers are presented in Figs. 4–7. The barrier height $B = 280$ meV. The diode consists of an n^+ source (at the left) and drain (at the right), each with doping $N_D = 10^{18} \text{ cm}^{-3}$, and an n channel, with doping $N_D = 5 \times 10^{15} \text{ cm}^{-3}$. The channel is 20 nm long, the barriers are 2.5 nm wide, and the quantum well between the barriers is 5 nm wide. There are 5 nm spacers between the barriers and the contacts.

Physical parameters for GaAs are electron effective mass $m = 0.063 m_e$, saturation velocity $v_s = 1.5 \times 10^7$ cm/s, dielectric constant $\epsilon = 12.9$, and relaxation time $\tau_{p0} = 0.072$ ps. The heat flux pre-factor is set to the canonical value $\kappa_0 = 2.5$.

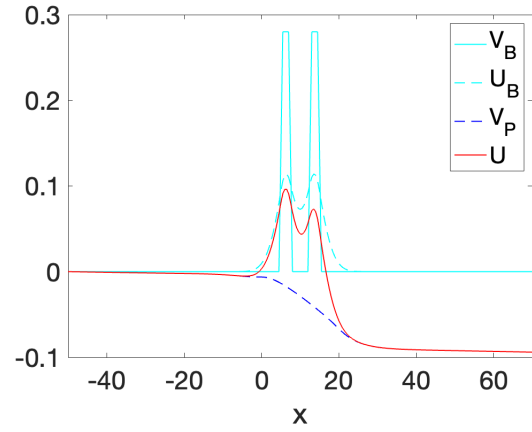


Fig. 5 The smooth potential U in eV for the resonant tunneling diode at the resonant peak with $V_{bias} = 94$ mV vs. x in nm.

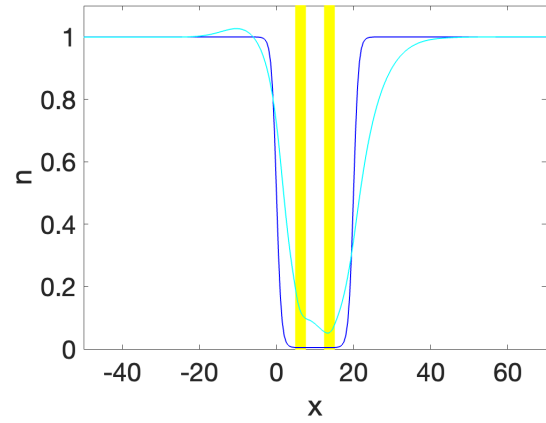


Fig. 6 Electron density n (cyan) and, for reference, doping density N_D (blue) in 10^{18} cm^{-3} vs. x in nm in the resonant tunneling diode at the resonant peak with $V_{bias} = 94$ mV.

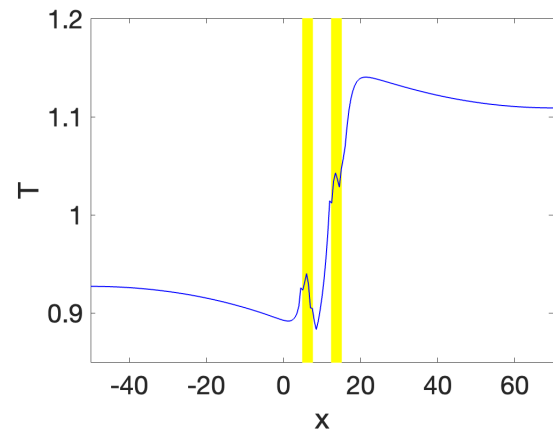


Fig. 7 Temperature T/T_0 vs. x in nm in the resonant tunneling diode at the resonant peak with $V_{bias} = 94$ mV.

Computational parameters for the resonant tunneling diode presented here are $CFL = 0.1$ and $\nu = 3$ (in our computational units: length scale = $0.1 \mu\text{m}$, energy scale = 1 eV , time scale = 0.1 ps , and density scale = 10^{18} cm^{-3}).

Figure 4 displays the experimental signal of quantum resonance: negative differential resistance in the current-voltage curve. Note that the smooth QHD simulation correctly predicts significant NDR in the resonant tunneling diode at 300 K, unlike the original QHD model.

The resonant peak of the current-voltage curve at 94 mV occurs as the electrons tunneling through the first barrier come into resonance with the energy levels of the quantum well, creating enhanced charge in the quantum well (see Figs. 5 and 6). As the voltage bias increases above 94 mV, the resonance effect rapidly decreases and then disappears because the effective right barrier height in U is progressively lowered.

Figure 7 illustrates that the electron gas cools as electrons encounter the channel and first quantum barrier, then heats up inside the well and at the channel/drain junction, and finally decays back toward ambient temperature in the drain.

5 Conclusion

We solved the underlying hyperbolic gas dynamical part of the time-dependent smooth QHD equations at 300 K using the third-order WENO method, treating the quantum mechanical, electric field, and relaxation time terms as source terms; the parabolic heat conduction and computational viscous terms using the TRBDF2 method; and the elliptic Poisson equation using PCG. These are the first time-dependent simulations of the smooth QHD model, and the first time-dependent simulations of any QHD model at 300 K.

By adding a computational viscosity term to the conservation of momentum equation (10), steady state is rapidly achieved by damping out the transient sound waves in the channel.

Since the TRBDF2 method is L-stable, timesteps are only restricted by desired accuracy and a relatively large Δt can be taken for the heat conduction and computational viscous terms, based on the CFL timestep constraint for the gas dynamical solver.

The explicit quantum term $-\hbar_{\beta}^2 n_x \bar{V}_{Bxx}$ in the momentum conservation equation (33) is essential in generating NDR. (The $-\hbar_{\beta}^2 (nu)_x \bar{V}_{Bxx}$ term in the energy conservation equation (34) goes to zero as steady state is approached.) To simulate quantum effects like charge buildup in quantum wells, only the $-nU_x$ and $-nuU_x$ quantum terms in (33) and (34), respectively, are needed (and convergence to steady state is rapid without the computational viscous term), but then NDR is not produced [7].

In summary, simulating the time-dependent smooth QHD model (for dynamic or steady state problems) provides an efficient way in which to incorporate quantum effects like resonant tunneling and charge buildup in quantum wells into the hydrodynamical depiction of charge transport in semiconductor devices.

Declarations

Funding: Not applicable

Conflicts of interest/Competing interests: Not applicable

Availability of data and material: Not applicable

Code availability: Custom code

References

1. A. ARNOLD AND A. JÜNGEL, *Multi-scale modeling of quantum semiconductor devices*, in Analysis, Modeling and Simulation of Multiscale Problems, Springer, Berlin, 2006, pp. 331–363.
2. G. BACCARANI AND M. R. WORDEMAN, *An investigation of steady-state velocity overshoot effects in Si and GaAs devices*, Solid State Electronics, 28 (1985), pp. 407–416.
3. R. E. BANK, W. M. COUGHRAN, W. FICHTNER, E. H. GROSSE, D. J. ROSE, AND R. K. SMITH, *Transient simulation of silicon devices and circuits*, IEEE Transactions on Computer-Aided Design, 4 (1985), pp. 436–451.
4. R. C. CHEN AND J. L. LIU, *A quantum corrected energy-transport model for nanoscale semiconductor devices*, Journal of Computational Physics, 204 (2005), pp. 131–156.
5. Z. CHEN, B. COCKBURN, C. L. GARDNER, AND J. W. JEROME, *Quantum hydrodynamic simulation of hysteresis in the resonant tunneling diode*, Journal of Computational Physics, 117 (1995), pp. 274–280.
6. C. L. GARDNER, *The quantum hydrodynamic model for semiconductor devices*, SIAM Journal on Applied Mathematics, 54 (1994), pp. 409–427.
7. C. L. GARDNER, *Quantum hydrodynamic simulation of hysteresis in the resonant tunneling diode at 300 K*, Journal of Computational Electronics, 20 (2021), pp. 230–236.
8. C. L. GARDNER, G. KLIMECK, AND C. RINGHOFER, *Smooth quantum hydrodynamic model vs. NEMO simulation of resonant tunneling diodes*, Journal of Computational Electronics, 3 (2004), pp. 95–102.
9. C. L. GARDNER AND C. RINGHOFER, *Smooth quantum potential for the hydrodynamic model*, Physical Review E, 53 (1996), pp. 157–167.
10. C. L. GARDNER AND C. RINGHOFER, *The Chapman-Enskog expansion and the quantum hydrodynamic model for semiconductor devices*, VLSI Design, 10 (2000), pp. 415–435.
11. C. L. GARDNER AND C. RINGHOFER, *Dispersive/hyperbolic hydrodynamic models for quantum transport (in semiconductor devices)*, in IMA Volumes in Mathematics and its Applications, vol. 136, Springer-Verlag, New York, 2003, pp. 91–106.
12. A. JÜNGEL AND S. TANG, *Numerical approximation of the viscous quantum hydrodynamic model for semiconductors*, Applied Numerical Mathematics, 56 (2006), pp. 899–915.
13. R. PINNAU, *A review on the quantum drift diffusion model*, Transport Theory and Statistical Physics, 31 (2002), pp. 367–395.
14. S. SHO AND S. ODANAKA, *Parallel domain decomposition methods for a quantum-corrected drift-diffusion model for MOSFET devices*, Computer Physics Communications, 237 (2019), pp. 8–16.

15. S. SHO, S. ODANAKA, AND A. HIROKI, *A simulation study of short channel effects with a QET model based on Fermi-Dirac statistics and nonparabolicity for high-mobility MOSFETs*, *Journal of Computational Electronics*, 15 (2016), pp. 76–83.
16. C.-W. SHU, *High order ENO and WENO schemes for computational fluid dynamics*, in *High-Order Methods for Computational Physics*, vol. 9 of *Lecture Notes in Computational Science and Engineering*, Springer Verlag, New York, 1999, pp. 439–582.
17. D. VASILESKA, S. M. GOODNICK, AND G. KLIMECK, *Computational Electronics: Semiclassical and Quantum Device Modeling and Simulation*, CRC Press, Taylor-Francis Group, Boca Raton, FL, 2010.
18. A. WETTSTEIN, A. SCHENK, AND W. FICHTNER, *Quantum device simulation with the density-gradient model on unstructured grids*, *IEEE Transactions on Electron Devices*, 48 (2001), pp. 279–284.